

## Optimised focusing ion optics for an ultracold deterministic single ion source targeting nm resolution

Robert Fickler<sup>a</sup>, Wolfgang Schnitzler<sup>a</sup>, Norbert M. Linke<sup>a,b</sup>, Ferdinand Schmidt-Kaler<sup>a</sup> and Kilian Singer<sup>a\*</sup>

<sup>a</sup>Institut für Quanteninformationsverarbeitung, Universität Ulm, Ulm, Germany; <sup>b</sup>Department of Physics, University of Oxford, Clarendon Laboratory, Oxford, UK

(Received 11 March 2009; final version received 11 July 2009)

Using a segmented ion trap with mK laser-cooled ions we have realised a novel single ion source which can deterministically deliver a wide range of ion species, isotopes or ionic molecules [Schnitzler et al. *Phys. Rev. Lett.* **2009**, *102*, 070501]. Experimental data is discussed in detail and compared with numerical simulations of ion trajectories. For the novel ion source we numerically investigate the influence of various extraction parameters on fluctuations in velocity and position of the beam. We present specialised ion optics and show from numerical simulations that a nm spatial resolution is achievable. The Paul trap, which is used as a single ion source, together with the presented ion optics, constitutes a promising candidate for a deterministic ion implantation method for applications in solid state quantum computing or classical nano-electronic devices.

**Keywords:** laser cooling; deterministic single ion source; ion optics

### 1. Motivation

Over the last few years, integrated semiconductor devices have reached structure sizes in the order of a few tens of nanometres, and further miniaturisation is expected. Thus, it is becoming more and more important to dope the devices in an exact predetermined and reproducible manner. In the next few years, the amount of doping atoms in the active region of a field effect transistor might drop below 100, then statistical Poissonian fluctuations which arise from conventional doping techniques will be significant. At nanometre length scales, only small fluctuations in the number of doped atoms are sufficient such that the assumption of homogeneously distributed doping atoms is no longer valid and the electronic characteristics are disturbed [1]. But not only conventional solid state devices would benefit from an accurate quantity of doping atoms, a future solid state quantum computer fully relies on precisely placed single dopant atoms; at well-defined distances and depths. In those quantum devices, single embedded impurity atoms, e.g. phosphorus dopants in silicon [2] or colour centres in diamond [3], are used to retain and process information in a quantum mechanical way. Nowadays it is possible to address single quantum devices like nitrogen-vacancy (NV) colour centres in diamond and to manipulate them coherently over several  $\mu\text{s}$  or even ms [4,5]. However, when it comes to scalable quantum computers with more than a few qubit carriers, one of the most important challenges

is to place the dopant atoms at an exact position and with uniform separation at nm resolution. One method proposed for the fabrication of these assemblies uses lithography based on scanning tunnelling microscopy (STM) [6–10]. A hydrogen terminated silicon surface is structured with an STM, followed by chemical reactive surface binding of the doping atoms. Although the positioning of the incorporated single phosphorous dopants is realised with sub-nm accuracy, the technique is limited to silicon surfaces and unavoidable impurities in the background gas can lead to functional impairment. Another method for controlling the amount of doping atoms is the direct implantation of atoms or ions. Here, the common approach utilises statistical thermal sources which provide a dense ion beam that has to be thinned out by several choppers and apertures. To ensure single ion implantation it is necessary to detect the implantation event by observing the generated Auger electrons, photoluminescence, phonons, electron–hole pairs or changes in the conductance of a field effect transistor [11–15]. Therefore, the implantation only works if the ions are either highly charged or implanted with large kinetic energies. With both systems it is possible to achieve a resolution of less than 10 nm, but their use is limited to cases where either highly charged states or high kinetic energies are available, and therefore deep implantation is unavoidable. Both methods lead to surface damage and additional inaccuracies in depth and lateral position

\*Corresponding author. Email: kilian.singer@uni-ulm.de

due to statistical straggling. Our method is universally applicable to a wide range of doping atoms and it allows implanting at very low energies, thus avoiding the problems described above.

## 2. Ultracold deterministic ion point source

We have realised a novel system for direct implantation of ions into solid state surfaces by using a Paul trap as an ultracold deterministic ion source [16–18].

### 2.1. Specialised linear Paul trap

Central component of our technique is a linear segmented Paul trap with laser cooled  $^{40}\text{Ca}^+$  ions similar to those utilised for scalable quantum information processing [19]. A Paul trap is a well known tool for trapping single, charged particles by using static (dc) electric fields and an alternating (rf) field, thereby producing a pseudo-potential of around 1 eV depth. With various laser cooling techniques, the trapped ions can be cooled to the motional ground state [20,21]. In addition, it is possible to trap other charged particles or even molecules that cannot be directly laser cooled but can be sympathetically cooled due to their electrostatic interaction. Identification of those additionally loaded doping ions, which are invisible to laser light, can be conducted by exciting collective vibrational modes [22,23]. The segmented trap design is capable of separating and transporting ions over a distance of a few cm [24]. Our design consists of four copper-plated polyimide blades of 410  $\mu\text{m}$  thickness and 65 mm length arranged in an x-shaped manner with a distance of 2 mm between opposing blades [18]. The dc voltages are applied to eight segments of 0.7 mm width on the top and bottom of each blade. A unique feature of our design is that it is capable of shooting out ions in a well-defined axial direction by switching two of the electrode segments to a higher voltage. Unlike conventional linear Paul traps, our design does not lose its radial confinement even when biasing the dc trap potential to high voltages. This is realised by applying the rf to the electrodes at the inner front edges of two opposing blades, while the other two are grounded. Furthermore, the trap features an additional broader deflection electrode on every blade, which is used to aim the extracted ions in the demanded direction. This special arrangement enables the exact axial extraction of the cooled  $^{40}\text{Ca}^+$  ions and sympathetically cooled dark ions due to the preservation of the radial confinement during the extraction sequence. The development and numerical investigation of this special design was feasible with our custom-designed simulation software (see Section 3). Characteristic working conditions are an rf voltage with

an amplitude of 200 V at a frequency of  $\Omega/2\pi = 12.155$  MHz, which yields a radial secular frequency  $\omega_{\text{rad}}/2\pi = 430$  kHz for a  $^{40}\text{Ca}^+$  ion. The required dc potential is generated by a voltage of 35 V which is applied to trap segments 2 and 8 and leads to a frequency of the axial potential of  $\omega_{\text{ax}}/2\pi = 280$  kHz. The vacuum chamber itself is made out of stainless steel and evacuated down to a base pressure of  $3 \times 10^{-9}$  mbar by a turbo molecular pump, an ion-getter pump and a titanium sublimation pump. Calcium and dopant ion generation is induced via a multiphoton process, e.g. by a pulsed frequency tripled Nd-YAG laser with a wavelength of 355 nm and a pulse power of 7 mJ.

### 2.2. Observation of ions

With this setup the trapped  $^{40}\text{Ca}^+$  ions are located above segment 5, where they are Doppler cooled and illuminated by laser light near 397, 866 and 854 nm. In order to image single ions or ion crystals we collect the scattered photons by a  $f/1.76$  lens on an electron multiplying charge coupled device (EMCCD) camera. While the calcium ions can be directly cooled by the installed laser system and identified on the image from the camera, the additionally loaded doping ions are sympathetically cooled and can be easily identified by the voids in the image of the ion crystal [18] as they are not excited by the applied laser fields at 397, 866 and 854 nm. By applying an alternating voltage to an electrode located under the ion crystal we can resonantly stimulate collective vibrational modes with characteristic resonance frequencies  $\omega_{\text{ax}}$  and therefore specify the exact species of these dark ions [22]. Another determination of the additionally loaded doping ions can be implemented by measuring the mass ratio with amplitude modulated resonant laser light [23]. So far, the trapped particles are simply Doppler cooled down to  $T \approx 2$  mK, which is slightly above the Doppler limit and was deduced from the width of the excitation spectrum on the  $S_{1/2}-P_{1/2}$  laser cooling transition. With further cooling methods using electromagnetically induced transparency, which is currently implemented in our lab, it is possible to cool the broad band of vibrational frequencies of an ion crystal simultaneously and thereby reach the motional ground state [20,25]. Under these initial conditions the ion trap would operate at the fundamental limit given by the Heisenberg uncertainty relation. In order to exclusively implant doping ions they can be separated from the cooling  $^{40}\text{Ca}^+$  ions in two different possible implementations. Firstly, by splitting the ions inside the trap before the extraction is performed and which can be achieved by converting the axial potential into a double well and transporting

the doping ion away by subsequently applying time dependent dc voltages [24]. The second possible separation process can be implemented after the extraction of the mixed ion crystal by deflecting unwanted ions, e.g. by increasing the voltage of an einzel-lens (see Section 3.2).

### 2.3. Extraction of ions

The extraction process itself is induced by biasing segments 4 and 5 with 500 V (supplied by Iseg Inc., Model EHQ-8010p) within a few nanoseconds. This fast switching is achieved by two high voltage switches (Behlke Inc., HTS 41-06-GSM) which are triggered by a TTL signal from our control computer. In addition, we synchronised the switching event with the rf field phase in order to reduce fluctuations of velocity and position of the ion by implementing an electronic phase synchronisation circuit which delays the TTL signal to a well-defined constant time period after the zero crossing of the rf. The experimentally measured standard deviation of the delay time equals 0.34 ns. For the detection of the extracted ions or dopants we use an electron multiplier tube (EMT) with 20 dynodes (ETP Inc., Model AF553) which is supplied with a voltage of  $-2.5$  kV and has a specified quantum efficiency of about 80% for positively charged particles. The gain is specified with  $5 \times 10^5$  and provides a 100 mV electrical signal which is 10 to 15 ns wide for each detection event. The EMT is accommodated in a second vacuum chamber which is located at 247 mm from the trap and can be completely separated by a valve to facilitate prospective changes of target probes.

### 3. Numerical simulation of the ion source and specialised ion optics

For designing an optimised trap and ion optics we developed a simulation software package which is based on a fast multipole solver [26,27] with additional high accuracy solvers respecting symmetry properties of the trap and the ion optics. The software allows deducing accurate electrostatic potentials from any CAD model. With this simulation software we describe the trajectories during the extraction and the expected spots at the target. We analyse the dependence of the spatial dimension and the velocity fluctuation of the single ion beam on the initial ion temperature, the start position inside the trap and the phase of the rf voltage at the extraction event. Additionally, we compare different designs of possible einzel-lenses and study the simulated focusing properties as well as the ability of our system to correct spherical aberration of the lens and to deflect the cooling ions during the implantation process.

To verify our simulation with experimental data we have checked different trap geometries and found an agreement of the axial and radial trapping frequencies within 2 to 3%.

#### 3.1. Deterministic ion point source

For an exact simulation of the trap potentials we have sketched the complete trap geometry as a full three-dimensional CAD model. By virtually applying the same voltages as we do in the real experiment (values mentioned above) we are able to calculate the trajectories of the trapped particles with full time dependent dynamics including micro motion at frequency  $\Omega$ . The initial momentum and position of the ion inside the trap is determined from the thermal Boltzmann distribution at a selectable temperature. The extraction process is triggered by switching two segments on every trap blade to 500 V synchronised to a well-defined phase of the rf voltage. The plotted trajectories show the influence of the micro motion during the extraction and the resulting spread of the ion beam (see Figure 1(a)). Slight numerical asymmetries, which appear despite the symmetrisation procedure, are corrected by small compensation voltages on the rails as in the real experiment.

##### 3.1.1. Dependence of the ion beam on the initial ion temperature

With an initial ion temperature of 2 mK the results show a  $1\sigma$ -spot<sup>1</sup> radius of  $16.5 \mu\text{m}$  at a distance of 247 mm between trap centre and target which amounts to a full angle beam divergence of  $134 \mu\text{rad}$  (see Figure 1(b)). The specified temperature of 2 mK is similar to the experimentally achieved value and the deflection electrodes are grounded during the extraction simulation. The mean longitudinal velocity of the extracted ions at the target is calculated to be  $22.1 \text{ km s}^{-1}$  with a  $1\sigma$ -uncertainty of only  $1.3 \text{ ms}^{-1}$ . Therefore, the predicted ion beam shows promising characteristics for subsequent focusing with ion optics due to small spherical and chromatical aberration. The predictions are even better if sub-Doppler cooling methods are applied. This would lead to mean phonon expectation values below 1 and temperatures of  $100 \mu\text{K}$  for the ions inside the trap, respectively. Then the setup would work at the Heisenberg limit. The full angle divergence of the generated ion beam shrinks to  $30 \mu\text{rad}$ . This means the  $1\sigma$ -spot size at the target amounts to  $3.7 \mu\text{m}$  and therefore the beam improves significantly. However, as the extraction voltage remains the same, the mean longitudinal velocity is not influenced by the smaller initial temperature, but the  $1\sigma$ -velocity uncertainty decreases slightly to  $1 \text{ ms}^{-1}$ . Although these values are

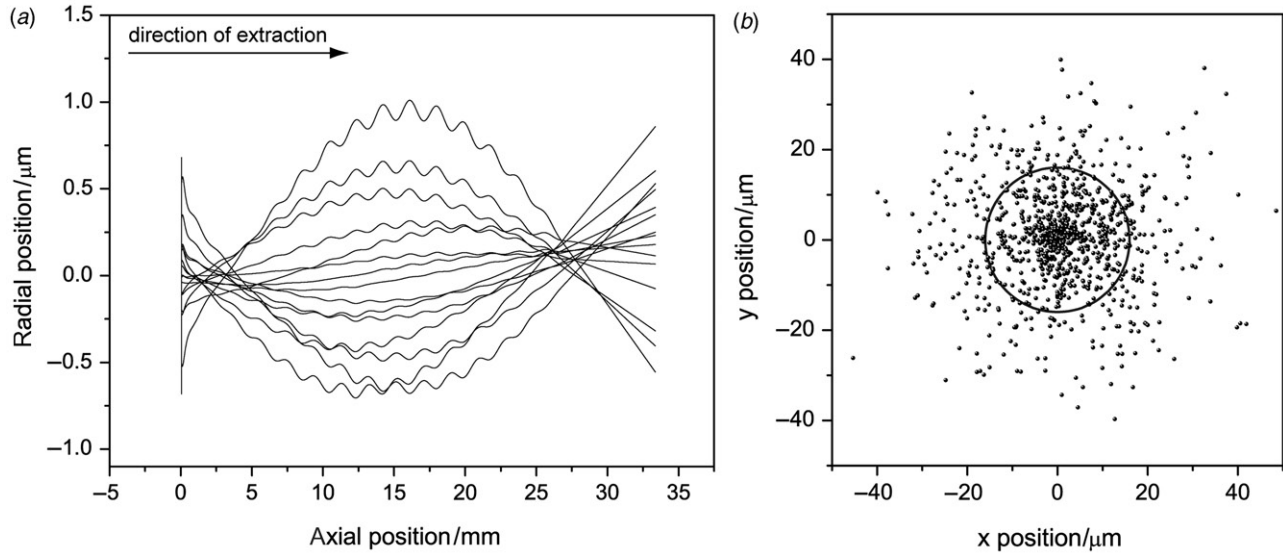


Figure 1. (a) Trajectories of  $^{40}\text{Ca}^+$  ions during extraction from the trap with an initial temperature of 2 mK. (b) Resulting spot diagram at a distance of 247 mm between trap centre and target amounts to a beam divergence of  $134\ \mu\text{rad}$  (grey circle illustrates the  $1\sigma$ -spot radius of  $16\ \mu\text{m}$ ).

very promising it has to be noted that these calculations are fully classical. As the ions are cooled to the motional ground state quantum mechanical simulations describing the propagation of the wave packets of the extracted ions would be needed to get more exact values. Nevertheless, these simulations show that by applying voltages to the deflection electrodes, the characteristics of the resulting spot shapes change enormously. For example, if we apply 7.5 V between two opposing deflection electrodes and 9.1 V between the others, respectively (which resembles our experimental setup), the spot is approximately shifted 19.4 mm in the horizontal and 30.5 mm in the vertical direction. In addition to this expected deflection the spot is stretched from the former Gaussian to a cigar-shaped distribution and therefore the  $1\sigma$ -spot size value cannot be calculated (see Section 3.1.3, Figure 3(b), zoomed area). This drastic change is simulated for 2 mK cooled ions as well as for sub-Doppler cooled ions.

### 3.1.2. Dependence of the ion beam on the initial start position

Aside from the dependence on the initial temperature, the transversal expansion and the velocity of the ion beam with its uncertainty strongly depends on the start position of the extracted ion. Whereas altering the initial position does not change the size and the (Gaussian) spot shape at the target significantly when deflection electrodes are grounded, the velocity fluctuation is strongly affected (see Figure 2(a)). For displacements up to  $\pm 400\ \mu\text{m}$  the mean longitudinal velocity for the different displacements has a constant

value of  $22\ \text{km s}^{-1}$  ( $\pm 2\%$ ). Conversely, the velocity spread at each displacement varies enormously: from only  $1.3\ \text{m s}^{-1}$  when the ions are extracted from the theoretical minimum of the axial potential, it increases up to  $1.5\ \text{km s}^{-1}$  when they are shifted around  $420\ \mu\text{m}$  out of the centre of the potential before being extracted. This is caused by a strong increase of the micro motion of a trapped ion when it is no longer in the minimum of the trapping potential, and therefore has a highly varying initial momentum. For the  $1\sigma$ -spot sizes it is also advantageous to extract the ion out of the potential minimum. Then, a  $1\sigma$ -spot of about  $16\ \mu\text{m}$  can be achieved. However, a displacement of  $\pm 400\ \mu\text{m}$  only leads to an enlargement of the  $1\sigma$ -spot size by an additional  $2\ \mu\text{m}$ . The influence of the start position on the ion beam properties becomes more crucial when the deflection electrodes are supplied with a non-zero voltage. Due to slightly displaced trajectories during the extraction process, the ions start to oscillate in the rf drive field and therefore lose their well-defined extraction direction. In Figure 2(a) the ions are displaced up to  $420\ \mu\text{m}$  from the potential minimum before extraction which means that the ion is trapped in the middle of two electrodes. The former cigar-shaped extension of the spot of around half a millimetre increases tremendously to about 10 to 20 mm. Additionally, the shape changes to a screw-like structure (see Figure 2(a)) and deterministic aiming becomes nearly impossible. The mean value of the longitudinal velocity sums to around  $22\ \text{km s}^{-1}$  and changes only by 2% for different extraction positions, while fluctuations increase to a maximum of  $1.6\ \text{km s}^{-1}$  for ions shifted  $420\ \mu\text{m}$  out of the trapping potential minimum.

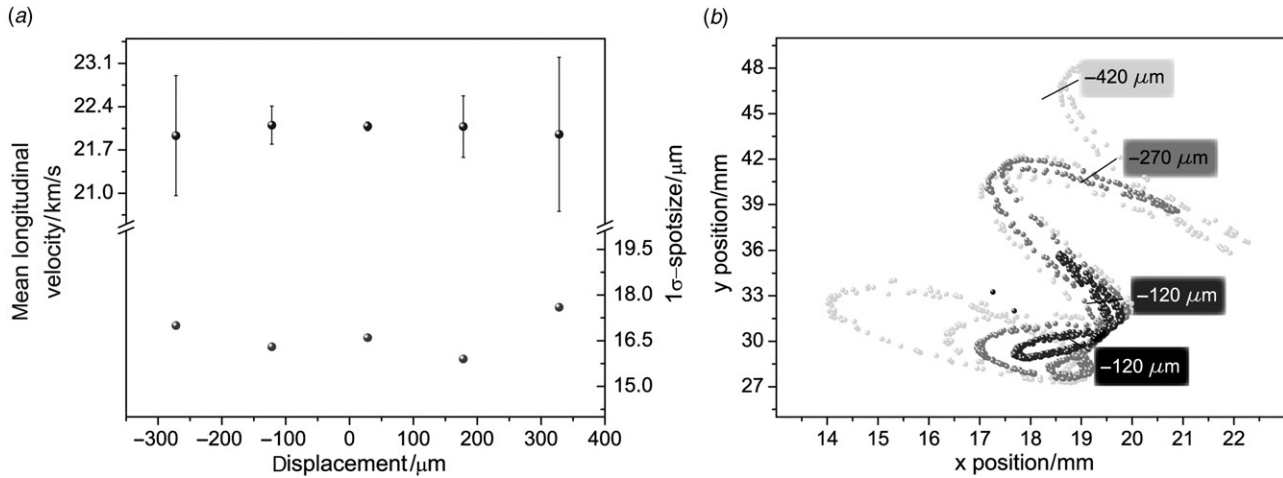


Figure 2. Dependence of the ion beam on the start position (positive values mean towards the extraction direction). (a) Resulting mean longitudinal velocities and  $1\sigma$ -spot sizes after extraction at a distance of 247 mm from the trap centre with deflection electrodes grounded. (b) Resulting spot diagrams of extracted ions when the deflection electrodes are biased to 7.5 V between two opposing trap blades and 9.1 V between the other two blades, respectively.

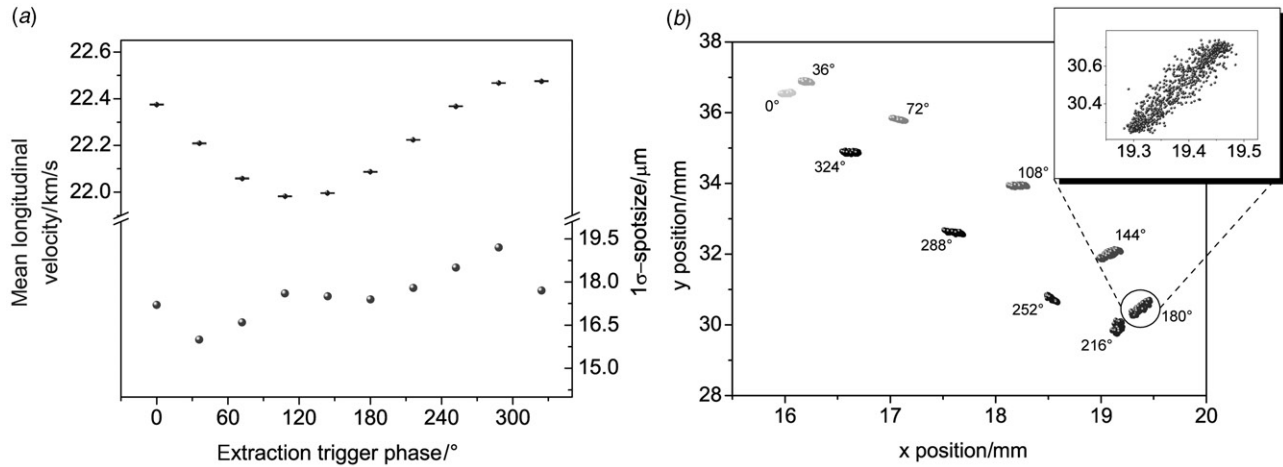


Figure 3. Dependence of the ion beam on the phase of the rf voltage. Initial temperature of the ions inside the trap is kept constant at 2 mK and the distance is set to 247 mm from the trap centre for all shown results. (a) Resulting mean longitudinal velocities and  $1\sigma$ -spot sizes with deflection electrodes grounded. (b) Resulting spot diagrams of extracted ion when the deflection electrodes are biased to 7.5 V between two opposing trap blades and 9.1 V between the other two blades, respectively. In (b) one spot is zoomed in to show that a Gaussian distribution is no longer an accurate assumption if the ions are deflected during extraction.

### 3.1.3. Dependence of the ion beam on the phase of the rf voltage at the instance of extraction

Similar results are calculated for the enlargement of the beam expansion while changing the phase of the rf voltage at the time of the extraction event (see Figure 3(b)). Here, the  $1\sigma$ -spot size varies from 16 to 19 μm over a whole period of the radio frequency voltage but remains Gaussian distributed. The mean longitudinal velocity oscillates in a sine-like manner over an interval of  $0.5 \text{ km s}^{-1}$  around  $22.2 \text{ km s}^{-1}$  during the different trigger phases. The velocity spread only varies negligibly between  $1.3$  and  $2.3 \text{ m s}^{-1}$ . This shows

that with deflection electrodes grounded, the trigger phase at the extraction event is important to reach a single ion beam featuring the promising characteristics of a narrow velocity fluctuation and a small beam divergence. Again, the exact triggering phase becomes even more important when the deflection electrodes are used to aim the ions during the extraction process. In Figure 3(b) the simulated spots are shown for altering the trigger phase and deflecting the ions with the same voltages mentioned above. The spot shape for a constant trigger phase maintains its oval shape and size. When changing the phase the spots are distributed over

an area of 10 mm by 15 mm. The mean velocity for each different trigger phase stays within 1% at around  $22 \text{ km s}^{-1}$ , and the fluctuations only add up to around  $2.5 \text{ m s}^{-1}$ . Hence, to achieve a beam of single deterministic extracted ions suitable for implantation it is important to align the trap axis to the ion optical axis as accurately as possible and therefore avoid the usage of the deflection electrodes. Besides the alignment, it is also crucial to position the ion into the radial pseudo-potential minimum. Furthermore, the extraction itself has to be synchronised to the rf field as exactly as possible.

### 3.2. Ion optics

In order to use our specially designed ion trap as a deterministic implantation tool it does not suffice to shoot the ions out of the trap with the aforementioned small values of beam divergence and velocity fluctuations: the ion trajectories have to be focused down to a few nm. To realise this goal we have developed ion optics which should be able to focus the beam down to the required nanometre regime, even to a  $1\sigma$ -spot size of around one nm without additional optical elements to reduce aberration errors. Due to the narrow ion trajectories and the low fluctuations in the velocity of the ions, the focusing optics can be kept simple without sophisticated aberration corrections [28–31]. A rotationally symmetric simple electrostatic einzel-lens yields adequate results. This type of ion lens consists of three electrodes where the first and the third electrode are on the same potential. The electrostatic potential resembles a saddle surface and can be generated in two different modes, decel-accel and accel-decel mode. The former mode is achieved when the middle electrode is biased to a voltage with the same sign as the charged particle (in our case a positive voltage) while the lens operates in the accel-decel mode with a voltage of opposite sign with respect to the charged particles. Both modes offer different advantages [32]. In the accel-decel mode the undesirable chromatical and spherical aberrations are smaller than in the decel-accel mode. The chromatic aberration is reduced due to higher velocities of the particles inside the lens and a therefore lower relative velocity spread  $\Delta v/v$ . Additionally, spherical aberration is smaller because the ion trajectories are closer to the optical axis during their passage through the lens [33] since they are always deflected towards the axis, while in the decel-accel mode the ions diverge at first before being focused to the centre. On the other hand, the decel-accel mode offers three essential advantages. Firstly, the lens requires lower centre electrode voltages for reaching a similar focal length. In addition,

by applying positive voltages it is possible to correct spherical aberration by switching the voltage to a higher potential while the particle is going through the lens [34] and in our setup the lens can be used as a deflector for different ion species (both will be discussed in more detail below).

#### 3.2.1. Comparison of different lens designs

In order to optimise the properties of the lens, different shapes are possible and have been discussed [31–33, 35, 36]. Generally, the most important feature is a perfect alignment of the electrodes in connection with voltage stability which depends, on the one hand, on the voltage supply, and on the other hand, on the insulating material between the electrodes. For the properties of the lens it can be presumed that the smaller the dimensions of the lens, the better its focusing properties are. However, the decreasing of the lens dimension is limited by the extension of the ion beam because spherical aberration effects become stronger when the size of the beam approaches the lens diameter. To assure that all ions easily go through the lens and spherical aberration is not dominant, we designed lenses with an entrance aperture of 1 mm. Usually the lens' properties improve when the first electrode is thinner than the second one and the gap spacing between them is minimal. Conversely, the distance between the second and the third electrode has to be much larger to minimise the focal spot size (see Figures 4(a) and (c)). Another possibility to improve the focusing properties is to change the shape of the electrodes, e.g. to a special design developed by Septier [36]. The design is based on a lens with hyperbolic field distribution which has good imaging characteristics even for steeply inclining beams, but has been modified to reduce spherical aberration (see Figure 4(b)). Each of the three electrodes has a different aperture and a completely different shape. For an optimal adjustment of the lens to our single ion source we have developed a huge range of different lenses and simulated the achievable spot sizes. In Figure 4 we present three different types to demonstrate the enormous influence of the lens design, each with the focal distance and the appropriate optimised focal spot size at different voltages and temperatures. A non-optimised einzel-lens made out of three equivalent electrodes and gaps in between in the decel-accel mode (see Figure 4(a)) allows one to focus down the non-deflected ion beam to a  $1\sigma$ -spot radius of 25.9 nm with 2 mK cooled ions (5.1 nm @ 100  $\mu$ K). Slightly better results are obtained in the accel-decel mode, where the  $1\sigma$ -spot size produces 20.7 nm for ion beams of 2 mK cooled ions (3.0 nm @ 100  $\mu$ K). Although this simple einzel-lens already achieves nanometre spot sizes, the required voltages, especially in the accel-decel mode, are

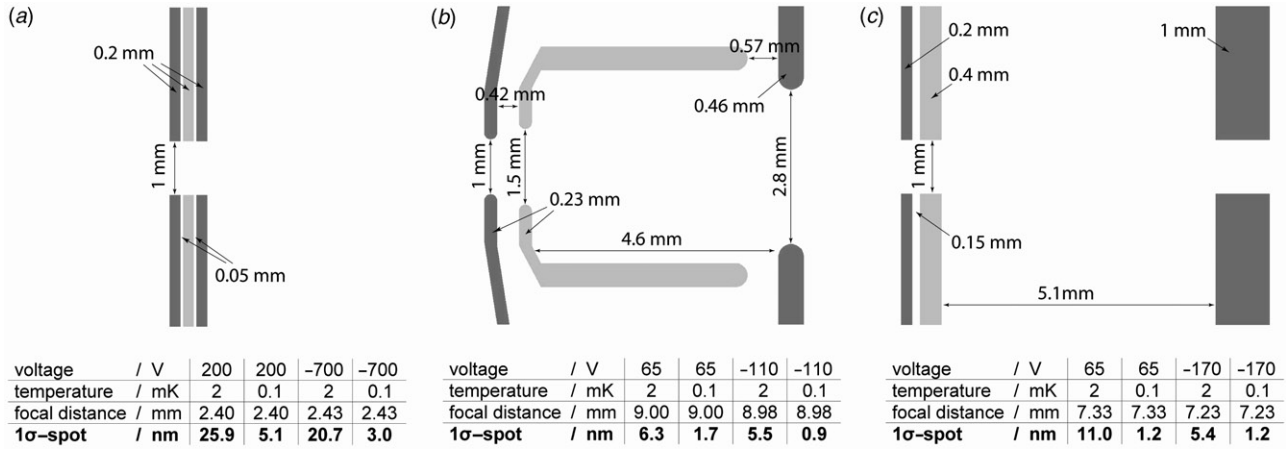


Figure 4. Comparison of three different shapes of einzel-lenses. Non-optimised simple lens (a) which is able to focus down the beam by a maximum factor of about 1200. Special shaped einzel-lens (b) with a design developed by Septier [36] where the minimal achievable  $1\sigma$ -spot size is more than three times smaller than the one of the non-optimised einzel-lens. Custom-made einzel-lens (c) which is implemented in our setup due to realisable electrode shapes with similar focusing properties as the special shaped lens (b). Aside from a maximum focusing factor of approximately 3000, the simulation predicts for the decel-accel mode (middle electrode repulsive) optimal results which is important for further implementation of spherical aberration correction and utilisation of the lens as an ion deflector. Voltages are applied to the centre electrode (light grey) while the outer ones are grounded (dark grey).

too high to ensure the insulating property of the spacer between the electrodes. Conversely, the lens in Figure 4(b), which resembles the one developed by Septier, is able to achieve (in decel-accel mode) a focal  $1\sigma$ -spot radius of 6.3 nm, even with ions of 2 mK temperature before extraction. With ions cooled to the motional ground state (100  $\mu$ K) the simulated spot size decreases down to 1.7 nm. Even better are the results for the accel-decel mode where the  $1\sigma$ -spot size amounts to 5.5 nm for 2 mK and only 0.9 nm for 100  $\mu$ K. This proves the desired qualities of our achieved ion beam and shows explicitly that our setup is able to operate at nm resolution. However, the realisation of this lens is quite difficult because of different apertures, the inclined electrodes and the rounded edges. For this reason we have developed a design with similar focusing properties but which is easily realisable (see Figure 4(c)).

### 3.2.2. Analysis of the developed einzel-lens

The apertures of all three electrodes of our developed einzel-lens equal 1 mm, which facilitates exact alignment. The gaps between the electrodes are 150  $\mu$ m wide to ensure the required insulation. For the accel-decel mode it is possible to reach a  $1\sigma$ -spot size of 1.2 nm for 100  $\mu$ K cooled ions (5.4 nm @ 2 mK) which is comparable to the results for the special shaped lens from Septier. Although the outcomes in the accel-decel mode for 2 mK are better than in the decel-accel mode, which means this mode shows bigger chromatical aberration effects, we have chosen to use the lens in the

decel-accel mode to be able to implement spherical aberration correction and to utilise the lens as a switchable deflector for ions. With 2 mK cooled ions inside the trap we can achieve a  $1\sigma$ -spot size of the extracted ions after focusing through the lens of 11.0 and 1.2 nm for ground state cooled ions, respectively.

In Figure 5, the induced potential for the lens of Figure 4(c) is plotted when the centre electrode is biased to 65 V. The potential plot illustrates the function of an einzel-lens in the decel-accel mode. Before the ions enter the lens, they are slowed down and deflected slightly away from the axis. After further defocusing, the ions reach the highest point of the potential which is approximately 60 V and therefore have the slowest velocity. Afterwards the ions are accelerated out of the lens and focused strongly to the axis. The focusing effect relies on the different ion velocities inside the lens potential. The longitudinal velocity of the ion is higher during the defocusing period while climbing to the maximum potential and it is lower during the focusing period thereafter. This generates the focusing force even for complete symmetric lens constructions as shown in Figure 4(a), and explains the lower voltages for lens designs where the focusing space is stretched by positioning the last electrode further away from the centre electrode (see Figures 4(b) and (c)). In Figure 6, trajectories of extracted  $^{40}\text{Ca}^+$  ions through the lens are shown, as well as the focal spot at a distance of 7.33 mm after entering the lens. When the ions are extracted with 2 mK initial temperature and the lens is biased to 65 V,

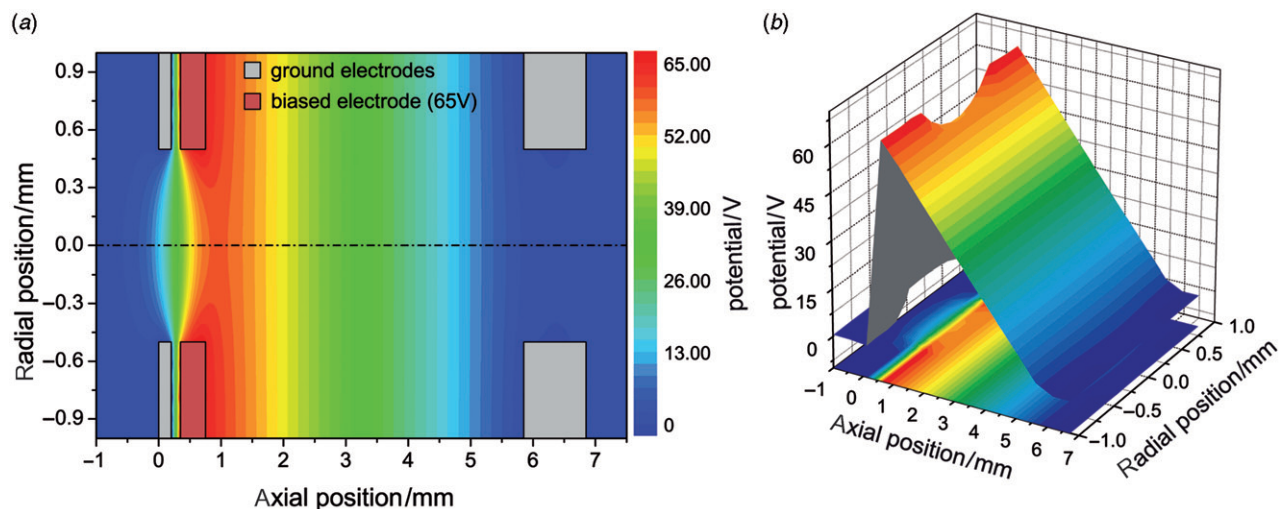


Figure 5. (a) Potential of the lens from Figure 4(c) where the central electrode is biased to 65 V. (b) Three-dimensional view of the potential distribution. (The colour version of this figure is included in the online version of the journal.)

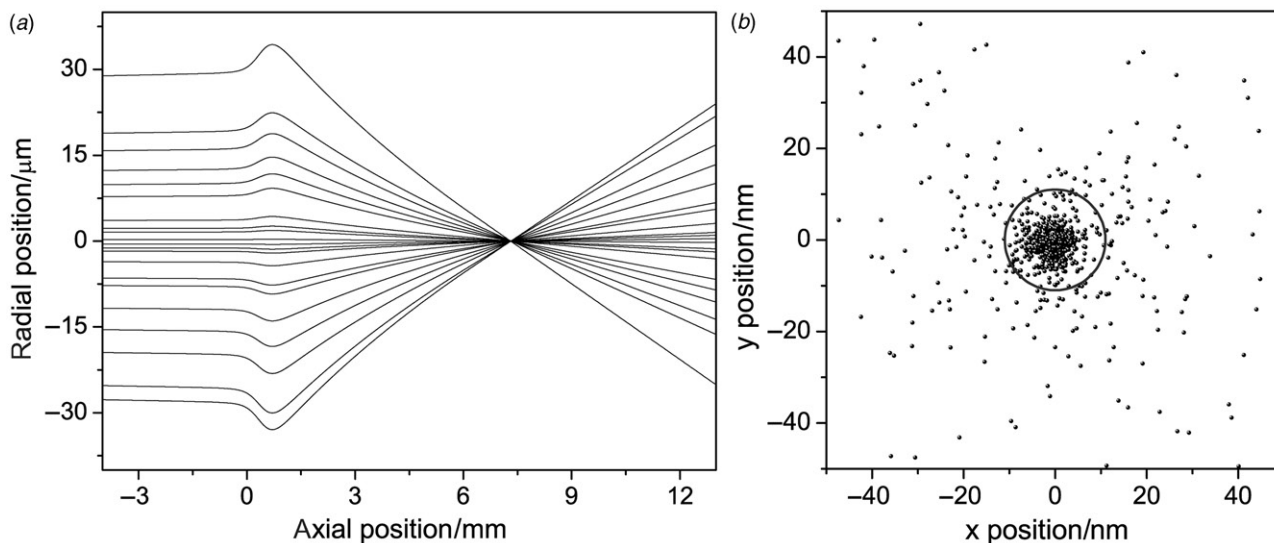


Figure 6. (a) Trajectories of extracted  $^{40}\text{Ca}^+$  ions at 2 mK which are focused by the lens of Figure 4(c) in the decel-accel mode (65 V) to a  $1\sigma$ -spot size of 11 nm. (b) Resulting spot diagram in the focal spot around 0.5 mm after the last electrode of the lens (grey circle illustrates the  $1\sigma$ -spot radius).

the focal spot occurs half a millimetre after the last electrode and shows a  $1\sigma$ -spot size of only 11 nm. Reducing the voltage of the centre electrode moves the focal spot size further behind the lens almost without impairment of the focusing properties. Lowering the voltage, for instance to 50 V, generates the spot 8.5 mm after the last electrode, but the spot size is hardly affected and remains at 12 nm. Therefore, the focal distance can be adjusted over a few mm without a severe loss in performance by simply changing the voltages of the centre electrode. However, the varying range should be as small as possible since further

decreasing of the voltage increases the spot size (see Figure 7(a)). A further reduction to 25 V, for example, enlarges the spot size up to 52 nm by a movement of around 100 mm. As described above, our ion source is able to deflect the ions during extraction by biasing the deflection electrodes. Small discrepancies in the alignment of the setup can be corrected by slight deflection of the beam into the optical axis. The importance of shooting through the lens without even small initial dislocation of the ion beam is shown in Figure 7(b). For example, a displacement of the incoming beam of half the aperture radius (250  $\mu\text{m}$ ) annihilates the

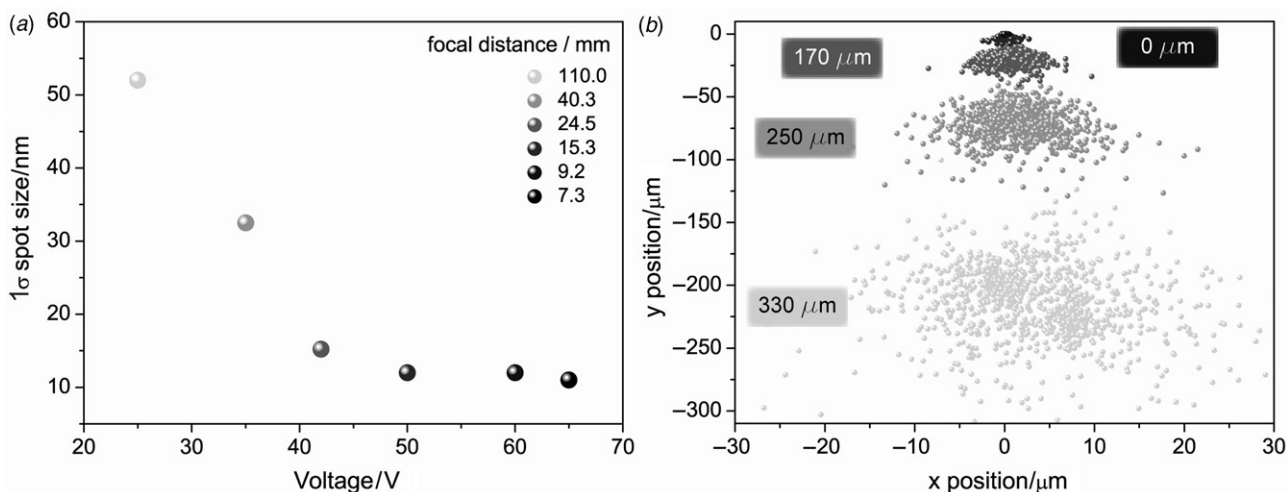


Figure 7. (a) Enlargement of the  $1\sigma$ -spot size by applying smaller voltages to the centre electrode of the lens. The focal plane moves away from the lens. 65 V is the upper limit for the lens voltage because even higher voltages would generate a focus of the beam inside the lens. (b) If the initial beam is dislocated out of the centre of the lens, the focusing properties of the lens worsen or even annihilate. Here, the focal plane is kept constant at 0.5 mm after the lens as well as the voltage of 65 V. The incoming beam is displaced upward in the positive  $x$ -axis to different distances.

focusing property. Besides the displacement of the outgoing beam in the opposite direction, it also diverges to similar spot dimensions as it has without any ion optics. With further shifting of the ion beam the lens even enlarges the spot size in the intended focal plane. Hence, for this required precise alignment, the deflection electrodes present the best way to aim the extracted ion beam to the centre of the lens aperture. A displacement in one direction of the trap axis of 250  $\mu\text{m}$  for example is neutralised by applying a potential of 0.36 V to two opposing trap blades and leads only to a small increase of the  $1\sigma$ -spot size from 16.1 to 17.2  $\mu\text{m}$ . However, when our setup is adjusted accurately, it is, in combination with the specially developed einzel-lens, a perfect implantation source, where nearly every species of charged particles or molecules can be deterministically implanted to any substrate with nanometre resolution.

### 3.2.3. Correction of the spherical aberration

One of the most advantageous properties of our setup is the fact that the ion extractions are synchronised to the rf voltage and the relative velocity uncertainty is extremely low. Thus, the ions are well defined in space and time during the whole extraction, as well as during the focusing process. With that, it is possible to switch the lens to different voltages at different points in time, which enables the correction of aberration effects. When compared to the lens from Septier our design shows a larger spherical aberration which enlarges the spot size a little bit. According to Scherzer's theorem,

it is not possible to avoid such spherical and chromatical aberration with rotationally symmetric electrostatic einzel-lenses in a charge free space [37]. Another way of interpreting the theorem is by stating the impossibility of the realisation of a diverging lens. One way of circumventing this theorem is to use time-dependent electrostatic fields [34] simply by switching the lens to another voltage at a well-defined time. This leads to forces a diverging lens would create and therefore spherical aberration can be reduced. Because of a fast increase of the lens potential at a well-defined time, the particle is accelerated and therefore slightly diverged. Ions with outer trajectories react stronger to the potential shift and subsequently intersect the optical axis further away. The switching time, where the lens voltage is altered from one value to another, has to be accurately chosen and has to be as short as possible. With our high voltage switches mentioned above we are able to vary the voltage within 5 ns, which is short enough to neglect additional energy broadening due to finite rise time of the electric field. However, the spherical aberration correction has to be adjusted to the incoming single ion beam. Simulation shows that for 2 mK cooled ions (which means a  $1\sigma$ -spot size of 16.1  $\mu\text{m}$ ) the best results are obtained when the lens is primarily grounded then biased to 60 V, 170 ns after the ions have passed the first aperture. Thus, the  $1\sigma$ -spot in the focal plane can be nearly reduced by a factor of 2 from 11 nm down to 6.0 nm. The same switching time and voltage reduces the focal  $1\sigma$ -spot size for ground state cooled ions from 1.2 to 0.9 nm. If the ion beam dimensions are

increased, the factor of improvement also increases slightly. For example, beam characteristics similar to the ones we expect in our experiment after perfectly aligning the lens axis to the trap axis ( $1\sigma$ -spot of  $36\ \mu\text{m}$  and a maximum velocity uncertainty of only  $6\ \text{ms}^{-1}$ ) requires a different setting for the switching time and voltage, but the reduction of the focal spot increases by more than a factor of 2 (see Figure 8). Here, the voltage is switched from 35 V during the entering of the ions to 85 V after 210 ns. The focused spot amounts to 138 nm when the lens is constantly biased to 65 V and decreased down to 57 nm for the spherical aberration corrected lens due to switching of the voltage (see Figure 8(c)). The remaining spread of the focal spot is therefore mainly due to the remaining chromatic aberration of the lens because of the velocity fluctuation. In order to show solely the enhancement of the correction of the spherical aberration, the velocity fluctuations have been artificially removed in Figures 8(a) and (b). Here, the spot improves with the spherical aberration correction from a  $1\sigma$ -spot size of 52 nm down to 12 nm. Note that the spot in Figure 8(a) does not show an accurate Gaussian distribution and therefore the measured value of 68% within 52 nm obviously cannot be read out from the plot. But Figures 8(a) and (b) give a good insight of the enhancement due to spherical aberration correction, whereas Figure 8(c) shows the effect of chromatic aberration. So far chromatic errors will not be corrected by the presented ion optics, but this can be also implemented with time-dependent electric fields [34].

### 3.2.4. Reflection of the cooling ions and post acceleration of the doping ions

Another advantage of the triggered extraction is the possibility to reflect the cooling ions during the implantation process. Because of unavoidable heating processes during a possible separation of the ions inside the trap [19], it is preferable to separate the cooling  $^{40}\text{Ca}^+$  ions from the implantation particles by reflecting the cooling ions at the einzel-lens. Due to different masses of the additionally loaded, sympathetically cooled ions compared to the  $^{40}\text{Ca}^+$  ions, the flight velocities differ from each other. Therefore, the cooling ions arrive at different times at the lens and can be easily reflected by applying higher voltages. Nitrogen, for instance, is accelerated in the simulation up to  $36.2\ \text{km s}^{-1}$  due to its smaller mass, and thus arrives approximately  $4.3\ \mu\text{s}$  earlier at the lens than the  $^{40}\text{Ca}^+$  ions. Hence, the lens has to be switched to a higher potential after the nitrogen particles have passed. The required voltage for reflection has to be at least 115 V, which is experimentally feasible (see Figure 9). Also worth mentioning is that post acceleration will even improve the focusing results by reducing the chromatical aberration due to a smaller *relative* velocity fluctuation. A simple cylindrical tube positioned in the ion beam axis and biased to 10 kV shows promising focusing effects when switched off after the ions are inside the tube. First simulated results predict velocities above  $200\ \text{km s}^{-1}$  and focal  $1\sigma$ -spot sizes of less than 0.4 nm for ground-state cooled ions. However, switching times have to be even more precise due to higher velocities and therefore shortened timescales.

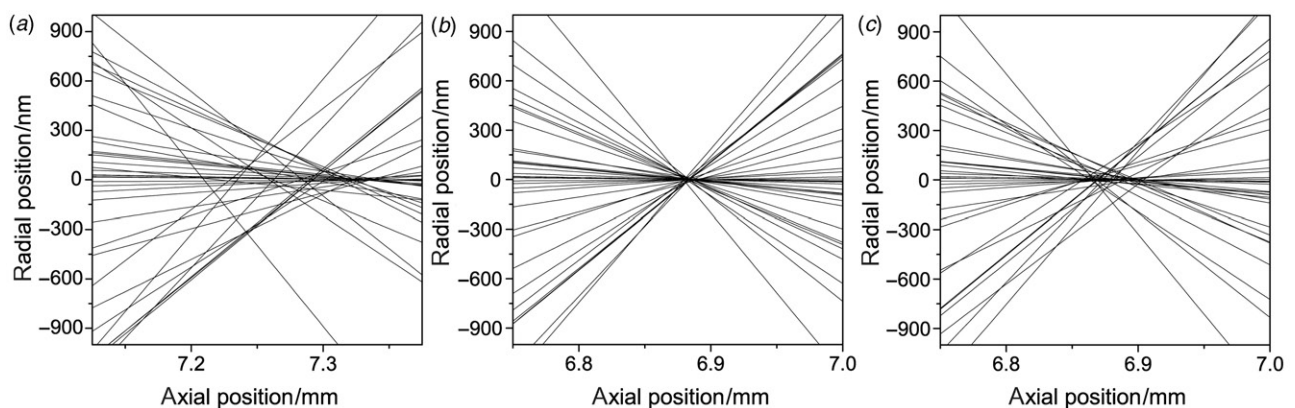


Figure 8. Zoom of the focal regions to show the effect of spherical aberration correction. All diagrams were calculated with an incoming beam with a  $1\sigma$ -spot radius of  $36\ \mu\text{m}$ . For the first two diagrams (a) and (b) the chromatical aberration effect is artificially removed by setting the velocity fluctuations of the ions to zero. The uncorrected spot (a) is achieved with the lens constantly being biased to 65 V and shows a  $1\sigma$ -spot radius of 52 nm. Conversely, the spherical corrected spot (b) only has  $1\sigma$ -size of 12 nm. 210 ns after the ions have entered the lens, the voltage of the centre electrode is switched from 35 to 85 V. The same incoming beam and correction settings of the lens are used for the trajectories in diagram (c), only with an added velocity fluctuation of  $6.3\ \text{ms}^{-1}$  to show the negative effect of the chromatic aberration of the lens. Here, 68% of all simulated ion trajectories lie within a spot radius of 57 nm.

Moreover, the gained reduction of the spatial resolution is partly neutralised by straggling effects of the implanted ions inside the target material.

#### 4. Experimental results of the novel ion source

We have implemented a linear segmented Paul trap as a novel ion source which is deterministic and has promising characteristics in velocity fluctuations and spot sizes for focusing the beam to nanometre resolution [18]. As mentioned above, the source has to be accurately synchronised to the phase of the rf trap drive voltage. We have therefore developed electronics that synchronise the TTL signal from the lab computer to the rf phase. The dependence of the hit rate on the extraction trigger phase is shown in Figure 10(a) where the detection probability has a maximum at a rf phase of around  $250^\circ$  to  $270^\circ$ . During all these measurements, the deflection voltages were kept constant and no additional apertures were placed in front of the detector (entrance aperture of the detector equals 20 mm). With smaller apertures, the contrast between detecting 90% of the extracted ions and missing the detector would be even stronger. Additionally, the experiment shows a weak dependence on the pressure in the vacuum chamber (see Figure 10(b)). When improving the vacuum down to a few  $10^{-9}$  mbar, the detection rate again improves to almost 90% as well. A linear extrapolation leads to a maximum detection probability of 92.5%. The dependency on the pressure is mainly based on possible collisions with the background residual gas particles. Furthermore, the stability of the ions in the trapping potential is lessened with higher pressure, which leads to higher fluctuations of the extraction trajectories. However, our measured hit rate lies above the specified quantum efficiency of 80% of the detector.

#### 4.1. Determination of the velocity fluctuation

In order to get information concerning the velocity fluctuation of the extracted ions we have measured the time of flight of each detected ion or ion crystal. The time of flight spectrum for ion crystals consisting of two ions is depicted in Figure 11(a). The difference between the arrival times of the first and the second ion results in  $\overline{\Delta t} = 26.3$  ns, which is mainly based on the Coulomb interaction. The spectrum shows that the ions remain in their crystalline structure during the extraction, which is important for the above-mentioned post-separation of the  $^{40}\text{Ca}^+$  ions from possible dopant ions or the implantation of a whole crystal with one extraction event. In order to characterise the spatial divergence of the ion beam, a movable aperture plate was installed in front of the detector. Along with this modification, a faster and more stable trigger phase electronic unit was also implemented. The subsequent measurements of the time of flight spectra are shown in Figure 11(b). With the improvement of the phase delay trigger the  $1\sigma$ -width reduces from the previous 50 ns down to 9.5 ns. The movement of the detector of about 30 mm further away from the trap causes an elongation of the time of flight from around  $12.7 \mu\text{s}$  up to  $14.74 \mu\text{s}$ . Therefore, the mean velocity of the extracted single  $^{40}\text{Ca}^+$  ions is measured to be  $19.47 \text{ km s}^{-1}$  with a  $1\sigma$ -width of  $6.3 (6) \text{ m s}^{-1}$ , meaning that the velocity uncertainty is a factor of 10 larger than inside the trap for the 2 mK cooled ions. The relative velocity uncertainty  $\Delta v/v$  is only  $3.2 \times 10^{-4}$  with the possibility of further reduction due to post-acceleration.

#### 4.2. Determination of the spatial beam dimension

The beam divergence is determined by scanning the beam over different apertures of 5 mm, 1 mm and

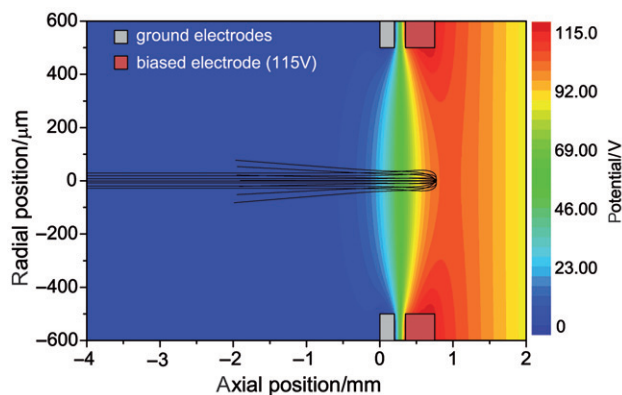


Figure 9. Trajectories of reflected  $^{40}\text{Ca}^+$  ions and potential distribution of the lens set to 115 V at the centre electrode (red). (The colour version of this figure is included in the online version of the journal.)

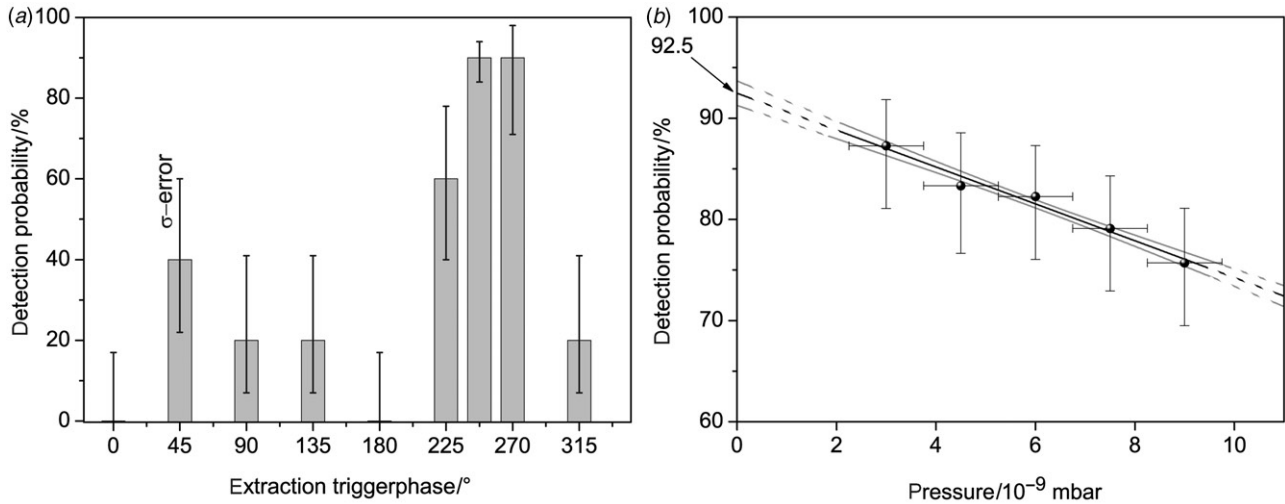


Figure 10. (a) Dependence of detection probability on different extraction trigger phases. (b) Detection probability during the extraction of single ions while the pressure changes. A linear fit is added (black line) as well as the standard deviation (grey line). The measurement is based on 251 successful extractions out of 310 shots. Both diagrams are measured without any aperture in front of the detector.

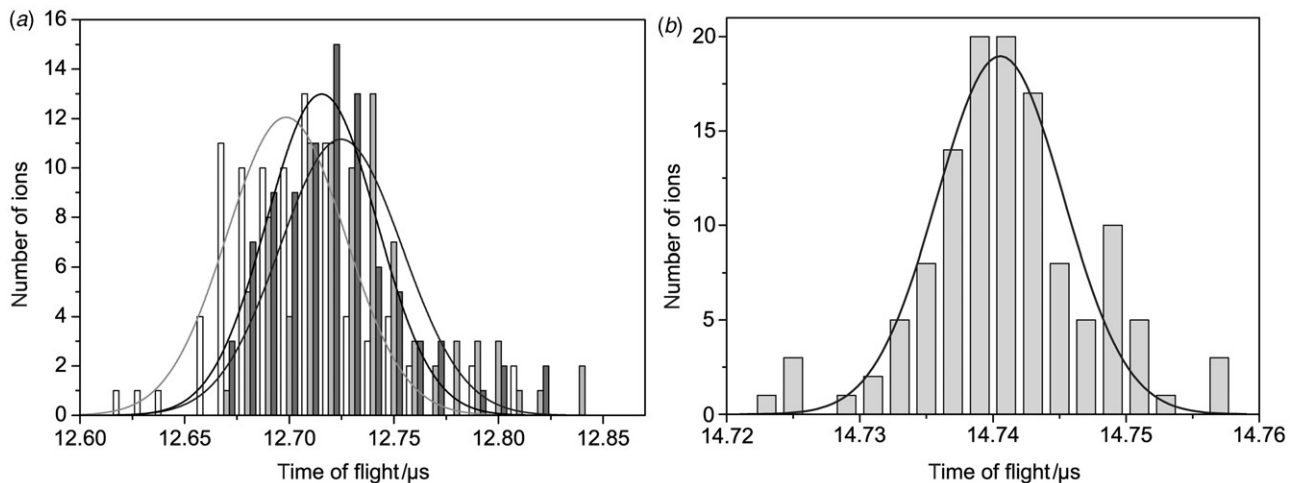


Figure 11. (a) Time of flight spectrum for two-ion crystals based on 93 successful detections without any aperture plates in front of the detector. The mean value for the first detected ion (white bins) amounts to  $12.699 \mu\text{s}$  with a  $1\sigma$ -spread of 56 ns (light grey line) and for the second ion (grey bins) to  $12.725 \mu\text{s}$  with a  $1\sigma$ -spread of 59 ns, respectively (grey line). The difference in arrival time between the first and the second ion amounts to  $\overline{\Delta t} = 26$  ns. Additionally, the mean value (dark grey bins) for the time of flight for both detection events adds up to  $12.715 \mu\text{s}$  with a  $1\sigma$ -spread of 52 ns (dark grey line). The bin size of the histogram is 10 ns. (b) Time of flight spectrum for single ion crystals based on 123 successful detections out of 139 shots through the 1 mm aperture. Gaussian fit of the data leads to an average time of  $14.74 \mu\text{s}$  with a  $1\sigma$ -spread of 9.5 ns. The bin size of the histogram equals 2 ns. Note that the different average times in (a) and (b) are caused by a repositioning of the detector backwards due to the installation of an aperture plate, and that the improvement of the  $1\sigma$ -spread is mainly due to the enhancement of the electronics of the phase delay trigger.

300  $\mu\text{m}$  diameter by altering the deflection voltages. Measurements conducted with the 5 mm aperture have shown that over a voltage range of 5 V between two opposing blades and 10 V between the other two opposing blades we are even able to detect ion crystals of up to 6 ions with an efficiency above 90%

(see Figure 12(a)). The edge of the aperture is also clearly recognisable in the scan diagram due to a sharp decrease of the detection rate. When reducing the aperture diameter to 1 mm the scanning range of the deflection voltages are scaled down to 1 and 2 V, respectively (see Figure 12(b)). In the centre of the

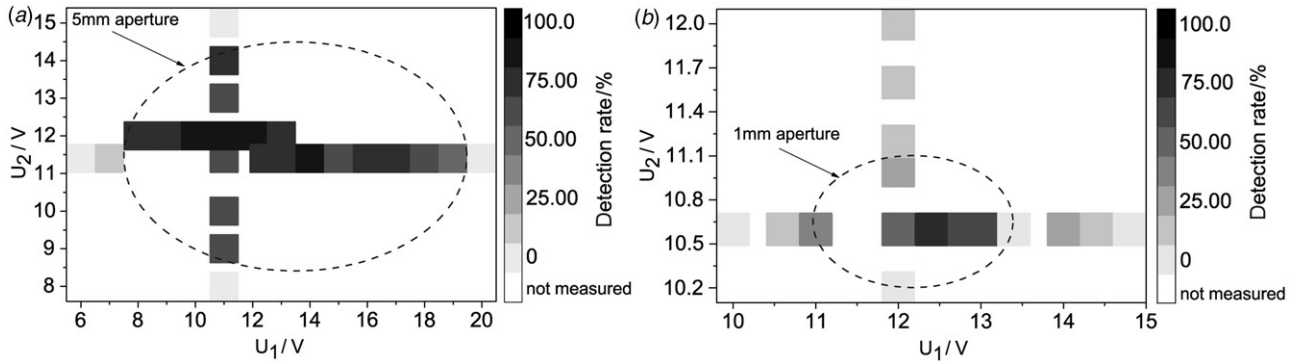


Figure 12. Detection probabilities as a function of the deflection voltages.  $U_1$  and  $U_2$  indicate the potential applied between two opposing blades. The scan clearly shows the edge of the aperture by a sharp decrease of the detection rate. (a) The range can be varied over 10 V and 5 V for the 5 mm aperture. (b) For the 1 mm hole the range where ions can be efficiently detected decreases to 2 and 1 V, respectively.

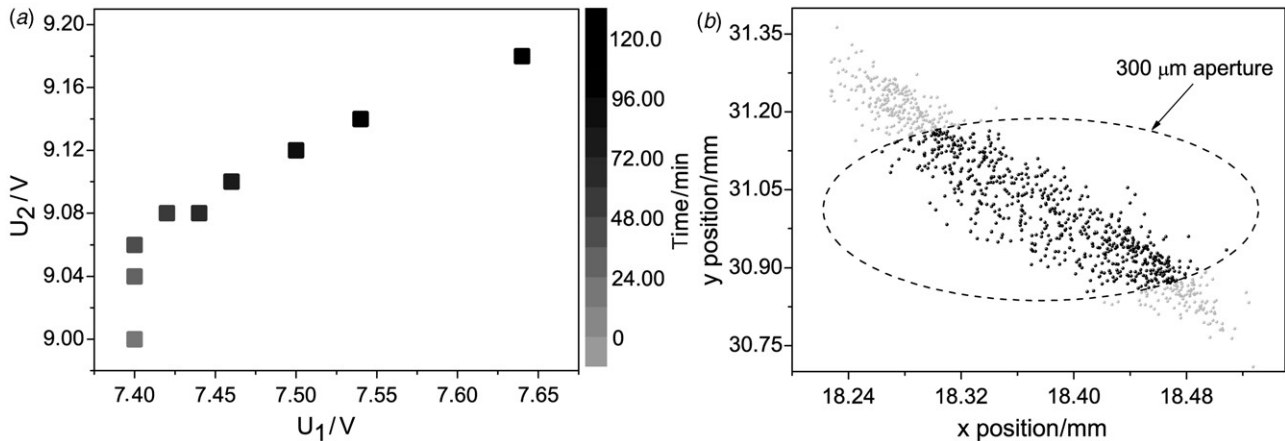


Figure 13. (a) Experimentally measured variation of optimal voltages  $U_1$  and  $U_2$  for the two pairs of opposing blades during measurements of two hours duration. The change in voltages compensates for the drift of the ion beam. Therefore, the detection probability could be kept constant at 68%. (b) Simulation of the spot with experimental settings. Black spots illustrate ions that would have passed the 300  $\mu\text{m}$  aperture whereas grey spots are blocked by the aperture. Therefore, 65% of the extracted ions can be detected after the aperture which is in good agreement with our experimental result (68%). Note that the spot is not a Gaussian distribution and is displaced by a few millimetres due to deflection voltages  $U_1 = 7.5$  V and  $U_2 = 9.1$  V.

scanned voltage range we detect 87% of the single extracted ions while the detection of ions which are extracted in a crystal shows a reduced detection rate of 78%. Note that the detection rate of nearly 90% for single ions lies above the specified quantum efficiency of the detector and is mainly limited by its performance. However, further downsizing of the dimension of the aperture to 300  $\mu\text{m}$  reduces the detection rate to 68% which indicates the cut-off of the spot by the edge of the aperture. By scanning over the 5 mm aperture at two different times we observed a drift of the ion beam of 15  $\mu\text{m min}^{-1}$ , possibly caused by temperature drifts or a displacement of the ions due to patch electric fields on the insulating surface between the electrodes. When using the 300  $\mu\text{m}$  aperture, the drift becomes more significant, which we compensated by adjusting the deflection voltages (see Figure 13).

### 4.3. Comparison of the experiment and the simulation

For a comparison of the experimental results with the findings from the simulations it is useful to obtain the simulated spot shape with all experimentally used settings. The resulting simulated spot again shows an oval shape. The velocities have a Gaussian distribution (similar to the experiment) with a  $1\sigma$ -spread of 2.7  $\text{m s}^{-1}$ . The experimentally measured values are by a factor of 2.2 larger than the simulated results. If it is assumed that the same holds true for the spatial spreading of the spot, it is possible to compare the results of the experiment and the simulation. With the cigar-shaped spot that is enlarged by a factor of 2.2, about 65% of the extracted ions would pass through the 300  $\mu\text{m}$  aperture (see Figure 13(b)). In our experiment we are able to detect 68% of the single ions

behind the 300  $\mu\text{m}$  hole, with adjustment of the deflection voltages during the extractions. From the simulation, we can also deduce that our trap is tilted by an angle of  $4.2^\circ$  at the  $x$ -axis and  $7.2^\circ$  for the  $y$ -axis.

## 5. Outlook

We have shown that our setup is able to deterministically extract single ions on demand. With additional optimised ion optics, the numerical simulation predicts a spot size with nm dimension. For an experimental confirmation of the predicted focal spot, different methods are conceivable. Similar to the previous measurements of the spatial beam divergence, it is possible to implement an aperture with less than 30 nm, which can be drilled, for example, by a focused ion beam (FIB) [16,17]. Another possibility to confirm the expected nm resolution of our combined system of ion trap and ion optics is to measure the achieved resolution after implanting the ions into solid state surfaces. With a STM, it is possible to identify subsurface impurities with nm resolution, produced by cobalt particles in a copper bulk material, for example [38]. A further method to confirm the resolution of single implanted ions makes use of generated NV colour centres in diamond [5]. Dipolar coupling of single nuclei localised close to the defect can be used to measure the achieved implantation resolution.

## Acknowledgements

We acknowledge financial support by the Landesstiftung Baden-Württemberg in the framework ‘atomics’ (Contract No. PN 63.14) and the ‘Eliteprogramm Postdoktorandinnen und Postdoktoranden’, the European commission within EMALI (Contract No. MRTN-CT-2006-035369) and the VolkswagenStiftung.

## Note

1. Note that the  $1\sigma$ -expression is always used to express that 68% of the studied data lies within the given interval, although some results are not perfectly reproduced by a Gaussian distribution.

## References

- [1] Shinada, T.; Okamoto, S.; Kobayashi, T.; Ohdomari, I. *Nature* **2005**, *437*, 1128–1131.
- [2] Kane, B.E. *Nature* **1998**, *393*, 133–137.
- [3] Greentree, A.D.; Fairchild, B.A.; Hossain, F.M.; Prawer, S. *Materials Today* **2008**, *11*, 22–31.
- [4] Gurudev Dutt, M.V.; Childress, L.; Jiang, L.; Togan, E.; Maze, J.; Jelezko, F.; Zibrov, A.S.; Hemmer, P.R.; Lukin, M.D. *Science* **2007**, *316*, 1312–1316.
- [5] Neumann, P.; Mizuochi, N.; Rempp, F.; Hemmer, P.; Watanabe, H.; Yamasaki, S.; Jacques, V.; Gaebel, T.; Jelezko, F.; Wrachtrup, J. *Science* **2008**, *320*, 1326–1329.
- [6] O’Brien, J.L.; Schofield, S.R.; Simmons, M.Y.; Clark, R.G.; Dzurak, A.S.; Curson, N.J.; Kane, B.E.; McAlpine, N.S.; Hawley, M.E.; Brown, G.W. *Phys. Rev. B* **2001**, *64*, 161401(R).
- [7] Schofield, S.R.; Curson, N.J.; Simmons, M.Y.; Ruess, F.J.; Hallam, T.; Oberbeck, L.; Clark, R.G. *Phys. Rev. Lett.* **2003**, *91*, 136104.
- [8] Ruess, F.J.; Oberbeck, L.; Simmons, M.Y.; Goh, K.E.J.; Hamilton, A.R.; Hallam, T.; Schofield, S.R.; Curson, N.J.; Clark, R.G. *Nano Lett.* **2004**, *4*, 1969–1973.
- [9] Pok, W.; Reusch, T.C.G.; Scappucci, G.; Rueb, F.J.; Hamilton, A.R.; Simmons, M.Y. *IEEE Trans. Nanotech.* **2007**, *6*, 213.
- [10] Ruess, F.J.; Pok, W.; Reusch, T.C.G.; Butcher, M.J.; Goh, K.E.J.; Oberbeck, L.; Scappucci, G.; Hamilton, A.R.; Simmons, M.Y. *Small* **2007**, *3*, 563–567.
- [11] Shinada, T.; Koyama, H.; Hinosihta, C.; Imamura, K.; Ohdomari, I. *Jpn. J. Appl. Phys.* **2002**, *41*, L287–L290.
- [12] Persaud, A.; Park, S.J.; Liddle, J.A.; Rangelow, I.W.; Bokor, J.; Keller, R.; Allen, F.I.; Schneider, D.H.; Schenkel, T. *QIP* **2004**, *3*, 233–245.
- [13] Mitic, M.; Andresen, S.E.; Yang, C.; Hopf, T.; Chan, V.; Gauja, E.; Hudson, F.E.; Buehler, T.M.; Brenner, R.; Ferguson, A.J.; Pakes, C.I.; Hearne, S.M.; Tamanyan, G.; Reilly, D.J.; Hamilton, A.R.; Jamieson, D.N.; Dzurak, A.S.; Clark, R.G. *Microelectron. Eng.* **2005**, *78*, 279–286.
- [14] Batra, A.; Weis, C.D.; Reijonen, J.; Persaud, A.; Schenkel, T.; Cabrini, S.; Lo, C.C.; Bokor, J. *Appl. Phys. Lett.* **2007**, *91*, 193502.
- [15] Shinada, T.; Kurosawa, T.; Nakayama, H.; Zhu, Y.; Hori, M.; Ohdomari, I. *Nanotechnology* **2008**, *19*, 345202.
- [16] Meijer, J.; Vogel, T.; Burchard, B.; Rangelow, I.W.; Bischoff, L.; Wrachtrup, J.; Domhan, M.; Jelezko, F.; Schnitzler, W.; Schulz, S.A.; Singer, K.; Schmidt-Kaler, F. *Appl. Phys. A* **2006**, *83*, 321–327.
- [17] Meijer, J.; Pezzagna, S.; Vogel, T.; Burchard, B.; Bukow, H.H.; Rangelow, I.W.; Sarov, Y.; Wiggers, H.; Plümel, I.; Jelezko, F.; Wrachtrup, J.; Schmidt-Kaler, F.; Schnitzler, W.; Singer, K. *Appl. Phys. A* **2008**, *91*, 567–571.
- [18] Schnitzler, W.; Linke, N.M.; Fickler, R.; Meijer, J.; Schmidt-Kaler, F.; Singer, K. *Phys. Rev. Lett.* **2009**, *102*, 070501.
- [19] Rowe, M.A.; Ben-Kish, A.; DeMarco, B.; Leibfried, D.; Meyer, V.; Beall, J.; Britton, J.; Hughes, J.; Itano, W.M.; Jelenkovic, B.; Langer, C.; Rosenband, T.; Wineland, D.J. *Quant. Inf. Comp.* **2002**, *2*, 257–271.
- [20] Roos, C.F.; Leibfried, D.; Mundt, A.; Schmidt-Kaler, F.; Eschner, J.; Blatt, R. *Phys. Rev. Lett.* **2000**, *85*, 5547–5550.
- [21] King, B.E.; Wood, C.S.; Myatt, C.J.; Turchette, Q.A.; Leibfried, D.; Itano, W.M.; Monroe, C.; Wineland, D.J. *Phys. Rev. Lett.* **1998**, *81*, 1525–1528.
- [22] Nägerl, H.; Blatt, R.; Eschner, J.; Schmidt-Kaler, F.; Leibfried, D. *Opt. Express* **1998**, *3*, 89–96.

- [23] Drewsen, M.; Mortensen, A.; Martinussen, R.; Staunum, P.; Sørensen, J.L. *Phys. Rev. Lett.* **2004**, *93*, 243201.
- [24] Huber, G.; Deuschle, T.; Schnitzler, W.; Reichle, R.; Singer, K.; Schmidt-Kaler, F. *New J. Phys.* **2008**, *10*, 013004.
- [25] Schmidt-Kaler, F.; Eschner, J.; Morigi, G.; Roos, C.F.; Leibfried, D.; Mundt, A.; Blatt, R. *Appl. Phys. B* **2001**, *73*, 807–814.
- [26] Greengard, L. *The Rapid Evaluation of Potential Fields in Particle Systems*; MIT Press: Cambridge, MA, 1988.
- [27] Nabors, K.; Korsmeyer, F.T.; Leighton, F.T.; White, J. *SIAM J. Sci. Stat. Comp.* **1994**, *15*, 713–735.
- [28] Weißbäcker, Ch.; Rose, H. *Jpn. Soc. Elec. Microscopy* **2001**, *50*, 383.
- [29] Weißbäcker, Ch.; Rose, H. *Jpn. Soc. Elec. Microscopy* **2002**, *51*, 45.
- [30] Szep, J.; Szilagy, M. *IEEE* **1988**, *35*, 1181–1183.
- [31] Hawkes, P.W.; Kasper, E. *Principles Of Electron Optics*; Academic Press: London, 1989.
- [32] Liebl, H. *Applied Charged Particle Optics*; Springer: Berlin, 2008.
- [33] Shimizu, K. *Jpn. J. Appl. Phys.* **1983**, *22*, 1623–1626.
- [34] Schönhense, G.; Spiecker, H. *J. Vac. Sci. Technol. B* **2002**, *20*, 2526–2534.
- [35] Riddle, G.H.N. *J. Vac. Sci. Technol.* **1978**, *15*, 857–860.
- [36] Septier, A. Septier CERN report: Aberation spherique de quelques lentilles electrostatiques a symetrie de revolution pour des faisceaux de grande ouverture; CERN Report, No. 60-39, Geneva, 1960.
- [37] Scherzer, O. *Z. Phys.* **1936**, *101*, 593–603.
- [38] Weismann, A.; Wenderoth, M.; Lounis, S.; Zahn, P.; Quaas, N.; Ulbrich, R.G.; Dederichs, P.H.; Blügel, S. *Science* **2009**, *323*, 1190–1193.